Available online at www.sciencedirect.com
ScienceDirect
Journal of the European Ceramic Society 31 (2011) 1811–1820
www.elsevier.com/locate/jeurceramsoc

Measurement of thermal residual stresses in ZrB_2–SiC composites

Jeremy Watts [a,*], Greg Hilmas [a], William G. Fahrenholtz [a], Don Brown [b], Bjorn Clausen [b]

[a] *Missouri University of Science and Technology, United States*
[b] *Lujan Center, Los Alamos National Laboratory, United States*

Received 31 December 2010; received in revised form 8 March 2011; accepted 14 March 2011
Available online 12 April 2011

Abstract

Neutron diffraction, Raman spectroscopy, and x-ray diffraction were employed to measure the stresses generated in the ZrB_2 matrix and SiC dispersed particulate phase in ZrB_2–30 vol% SiC composites produced by hot pressing at 1900 °C. Neutron diffraction measurements indicated that stresses begin to accumulate at ~1400 °C during cooling from the processing temperature and increased to 880 MPa compressive in the SiC phase and 450 MPa tensile in the ZrB_2 phase at room temperature. Stresses measured via Raman spectroscopy revealed the stress in SiC particles on the surface of the composite was ~390 MPa compressive, which is ~40% of that measured in the bulk by neutron diffraction. Grazing incidence x-ray diffraction was performed to further characterize the stress state in SiC particles near the surface. Using this technique, an average compressive stress of 350 MPa was measured in the SiC phase, which is in good agreement with that measured by Raman spectroscopy.

Keywords: Borides; SiC; Residual stress; Composites; Neutron diffraction

1. Introduction

Zirconium diboride (ZrB_2) is one of a group of metal boride compounds known as ultra-high temperature ceramics (UHTCs), which exhibit melting temperatures in excess of 3000 °C.[1,2] In addition to their high melting point, the metal borides are generally resistant to chemical attack.[3] Additionally, ZrB_2 composites, specifically those produced using silicon carbide (SiC) as a uniformly dispersed second phase, display a wide variety of desirable properties. Flexural strengths have been reported in excess of 1000 MPa.[4–6] The addition of SiC increases fracture toughness from ~3.5 MPa/m$^{1/2}$ for monolithic ZrB_2[4] to as much as 5–6 MPa/m$^{1/2}$ for ZrB_2 with additions of 20–30 vol% of SiC particles.[4,7] Composites of ZrB_2 and SiC also exhibit increased oxidation resistance over that of monolithic ZrB_2 by producing a silica containing glassy layer on the surface which slows the rate of further oxidation at temperatures above ~1100 °C.[2,8–13] Both pure ZrB_2 and ZrB_2–SiC composites have been shown to posses thermal conductivities above 60 W/m K.[14] This combination of properties has made ZrB_2–SiC composites attractive candidates for future aerospace applications.[15–17]

For ZrB_2–SiC composites, the mismatch in the coefficient of thermal expansion (CTE) between the ZrB_2 matrix and the dispersed SiC particulate phase results in the generation of residual stresses in both phases during cooling after densification at elevated temperatures. Further, the residual stresses would be expected to play a significant role in controlling the thermal and mechanical properties, as well as the behavior of ZrB_2–SiC composites as a function of temperature. The CTE of ZrB_2 is approximately 2 ppm/K higher than that of the 6H polytype of α-SiC over the temperature range being tested (room temperature to 1750 °C). Specifically, ZrB_2 has a CTE of ~5.2 ppm/K at 298 K,[2,18] while SiC is ~3.3 ppm/K at 298 K.[18] Because of the CTE mismatch, as ZrB_2–SiC composites are cooled from their final densification temperature (typically >1800 °C) the matrix tries to shrink at a faster rate than the SiC particles. The result, after cooling to room temperature, is a tensile stress state in the ZrB_2 matrix and a corresponding compressive stress state in the SiC particulate phase.

One analytical technique that has been used for measuring residual stresses in ceramics is neutron diffraction.[19–22] Neutron diffraction is preferable to standard x-ray diffraction in this case because neutrons are capable of probing the entire

* Corresponding author.
E-mail address: jwatts@mst.edu (J. Watts).

0955-2219/$ – see front matter © 2011 Elsevier Ltd. All rights reserved.
doi:10.1016/j.jeurceramsoc.2011.03.024

volume of a sample.[23] For comparison, typical x-ray diffraction studies that use Cu Kα radiation would penetrate a maximum of ~50 μm into a ZrB_2–SiC composite according to Eqs. (10) and (11) which will be discussed in detail below. For diffraction studies, residual stresses in composite materials are calculated by comparing the lattice parameters of pure, stress free constituents of a given composite (typically powders) to those of the matrix and dispersed second phase in a composite after processing. Using the appropriate elastic moduli for the phases, the lattice parameter changes (strains) can be converted to internal stresses.

Raman spectroscopy is another method for measuring the residual thermal stresses in Raman active materials. Raman spectroscopy uses scattered light (usually visible wavelength laser light) to probe the vibrational energy levels of chemical bonds.[24] Similar to other forms of spectroscopy, Raman patterns are specific to a compound or molecule, which allows for its use in phase identification. In addition to Raman peaks being unique to a particular compound, the absolute position of Raman peaks is sensitive to stress.[25–29] While no universal correlation between Raman peak position and stress has been identified, various materials have been examined under known stresses to correlate peak shift to stress.[26,28,30,31] Raman spectroscopy is limited, however, by the fact that not all materials exhibit Raman scattering. It is also a surface sensitive technique for materials that are opaque to the incident light.

In a recent study, neutron diffraction was used to measure the thermal residual stresses in ZrB_2–SiC composites.[22] The composite material used in that study was produced by attrition milling the starting powders with tungsten carbide (WC) media. As a result, the final composites contained a small amount of WC contamination (~4 wt%).[22] During the neutron diffraction experiments at elevated temperatures, the W contamination that was initially present as a solid solution with the ZrB_2 matrix came out of solution, which altered the ZrB_2 lattice parameter. As a result, it was not possible to decouple the change in lattice parameter due to the chemical change and that due to thermal stresses, meaning that the stress in the ZrB_2 matrix could not be calculated from the data. The goal of the current study was to measure the thermally induced residual stresses in ZrB_2–SiC composites using both neutron diffraction and Raman spectroscopy for materials free of any W contamination. Special samples had to be prepared for use in neutron diffraction. Naturally occurring boron consists of ~80% boron-11 (^{11}B) and ~20% boron-10 (^{10}B); the high neutron absorption cross section of ^{10}B (3835 barn)[32] causes low diffracted beam intensity making neutron diffraction impractical in ceramics containing natural boron. However, the neutron absorption cross section of ^{11}B is 0.0055 barn.[32] In order to take advantage of the low absorption cross section of ^{11}B, samples were produced via reactive hot pressing using ZrH_2 and ^{11}B powder precursors to produce $Zr^{11}B_2$ based composites suitable for neutron diffraction. Three samples were prepared for neutron diffraction: pure $Zr^{11}B_2$ powder, pure SiC powder, and a dense composite consisting of 70 vol% $Zr^{11}B_2$ and 30 vol% SiC. To determine the total magnitude of residual stresses within the composite, as well as the temperature at which stresses began to accumulate on cooling, neutron diffraction patterns were collected at temperature intervals ranging from 1750 °C down to room temperature. To complement the neutron diffraction data, stress measurements were also made using Raman spectroscopy by examining individual SiC particles within the composite microstructure.

2. Experimental procedure

The ZrB_2–SiC particulate composites used in the current study were prepared via a reactive route to control the isotopic content of boron in the material. The composite was prepared from ZrH_2 (Alfa Aesar, Grade Z-1038, Ward Hill, MA, USA), boron (Ceradyne Boron Products, Isotopic enriched boron 11 metal, Quapaw, OK, USA) and SiC powders (H.C. Starck, Grade UF-25, Goslar, Germany). The SiC powder was an α-SiC consisting primarily of the 6H polytype. An appropriate amount of each powder was used to produce a 70 vol% $Zr^{11}B_2$–30 vol% SiC composite. The powders were attrition milled using a fluoropolymer lined vessel, acetone as the liquid medium, and SiC milling media (4.7 mm diameter SiC satellites, Union Process, Akron, OH, USA). The powders were attrition milled for 2 h to reduce particle size and to intimately mix the powders to facilitate later reaction. Following attrition milling the slurry was rotary evaporated to remove the acetone and minimize preferential settling. At this stage, an effort was made to limit the exposure of the powder to air as both the ZrH_2 and ^{11}B powders are reactive with oxygen and moisture in the atmosphere. The newly formed surfaces from milling serve to increase their reactivity further. Following solvent removal, the dried powder was passed through a 60 mesh sieve to facilitate uniform die filling for hot pressing.

The composite was hot pressed in a graphite die to produce a sample ~44 mm in diameter prior to sectioning. The die wall, as well as the ends of the die rams, was coated with graphite paper (Graphoil, GTA grade, Leader Global Technologies, Deer Park, TX, USA). The ends of the die rams, which would be in contact with the powder, were also coated with a boron nitride spray (Cerac, SP-108, Milwaukee, WI, USA) to prevent reaction with the graphite. The powder was loaded in the die and cold compacted to ~6 MPa. Densification was achieved using a resistively heated graphite element hot press (Thermal Technology Inc., Model HP20-3060-20, Santa Rosa, CA, USA). Below 1650 °C the powder compact was heated under vacuum (~25 Pa). The powder was heated at ~5 °C/min up to 700 °C to allow the ZrH_2 and ^{11}B to react and form $Zr^{11}B_2$. The compact was then heated at ~75 °C/min to 1450 °C and 1650 °C, with 1 h holds at each temperature to facilitate the removal of oxide species from the surfaces of the powders. Following the hold at 1650 °C the atmosphere was changed from vacuum to argon, 32 MPa of uniaxial pressure was applied, and the sample was heated at ~50 °C/min to 1900 °C. Once reaching 1900 °C the hydraulic ram travel was monitored to determine the extent of densification. Once ram travel had ceased, the furnace power was turned off and the sample allowed to cool (~50 °C/min from 1900 °C to below 600 °C) to room temperature. Pressure was maintained on the sample until the temperature fell below 1650 °C. Following densification the hot pressed sample was removed from the

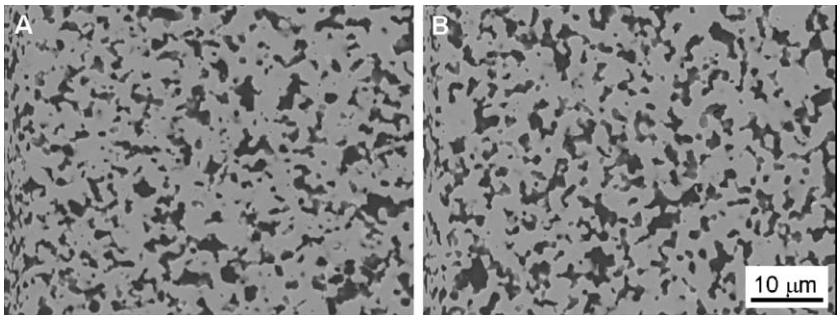

Fig. 1. SEM images showing the microstructure of neutron diffraction specimen (A) before and (B) after the experiment showing no obvious change in microstructure.

die and surface ground on both sides to remove any graphite or boron nitride adhering to the sample. A specimen approximately 4.2 mm × 5.2 mm × 30 mm was sectioned out of the hot pressed sample for the neutron diffraction experiment.

Stress measurements were performed by neutron diffraction, Raman spectroscopy, and x-ray diffraction. Neutron diffraction was performed using the time of flight (TOF) method on the Spectrometer for Materials Research at Temperature and Stress (SMARTS) in the Lujan neutron scattering center at Los Alamos National Laboratory. The 70 vol% $Zr^{11}B_2$–30 vol% SiC composite specimen (4.2 mm × 5.2 mm × 30 mm) was positioned vertically in a graphite holder within a tungsten element furnace situated such that only the specimen was exposed to the neutron beam. The specimen was heated under vacuum ($\sim 1.3 \times 10^{-3}$ Pa) to a maximum temperature of 1750 °C at a rate of 20 °C/min. Neutron diffraction patterns were collected at regular temperature intervals ranging from room temperature to 1750 °C during both heating and cooling cycles. The temperature was allowed to equilibrate for 15 min prior to each measurement. Diffraction data was then collected for approximately 1 h at each temperature. The same procedure was followed to measure both pure $Zr^{11}B_2$ and SiC powders, except that the powders were contained in a niobium crucible. The data collected on heating was indistinguishable from that gathered on cooling; for the purposes of this study the cooling data was used for subsequent measurements and calculations. Single peak fitting as well as whole pattern fitting was performed using the General Structure Analysis System (GSAS) software package.[33] Raman measurements were made using a Raman spectrometer (Horiba LabRAM ARAMIS, Edison, NJ, USA) employing a 633 nm HeNe laser and a 1 μm spot size. Prior to collecting data, the instrument was calibrated using a silicon standard and the main silicon peak at 520.0 cm^{-1}. Raman patterns were acquired only from the SiC particles within the microstructure since ZrB_2 is not Raman active. Spectra were acquired from 25 individual SiC particles from the surface of the specimen. X-ray diffraction was performed using a grazing incidence diffractometer (PANalytical, X-Pert, Almelo, The Netherlands). The source was set at an angle of incidence of 1° to the surface of the specimen, and the detector was moved to scan the range from 5° to 90° 2θ. Specimens of the $Zr^{11}B_2$–SiC composite, as well as of the pure SiC powder, were measured. Single peak fitting was employed to determine peak shifts between the powder and composite.

Microstructural images were obtained by scanning electron microscopy (SEM) (Hitachi, S570, Tokyo, Japan). Specimens were polished to a 0.25 μm finish using diamond abrasives. Image analysis was performed using ImageJ software (National Institutes of Health, Bethesda, MD, USA).

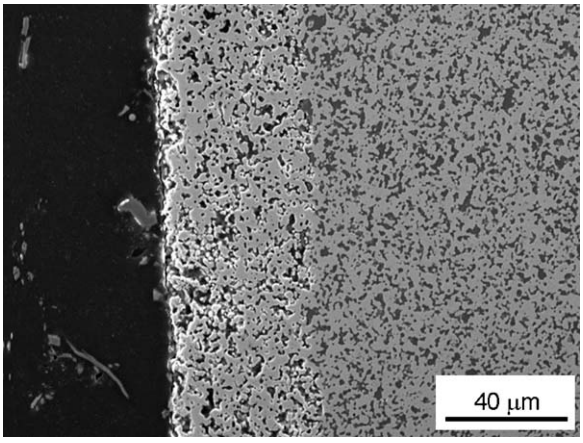

Fig. 2. SEM image showing the outer edge of a neutron diffraction specimen after testing, revealing a surface layer ~50 μm thick depleted of SiC due to active oxidation.

3. Results and discussion

The neutron diffraction experiment involved holding the specimen at elevated temperatures (as high as 1750 °C) for extended periods of time; therefore, the microstructure of the specimen was examined using SEM both before and after neutron diffraction to determine whether or not the experiment affected the microstructure (Fig. 1). The micrographs indicate homogenous microstructures consisting of a $Zr^{11}B_2$ matrix (the light grey phase) with uniformly dispersed SiC particles (the dark phase). It is important that the microstructure of the specimens does not change during the neutron diffraction experiment. Grain growth of either phase, or coalescence of the dispersed SiC particulate phase, could generate or alleviate stresses independent of the thermal cycle. The microstructures in Fig. 1 are indistinguishable from one another; this in addition to the lack of any additional phases detected via neutron diffraction indicate that the measured lattice parameter shifts were likely due to temperature effects and not other microstructural changes. It should be noted that the outermost surface of the specimens was affected by extended holds at elevated temperature, and in par-

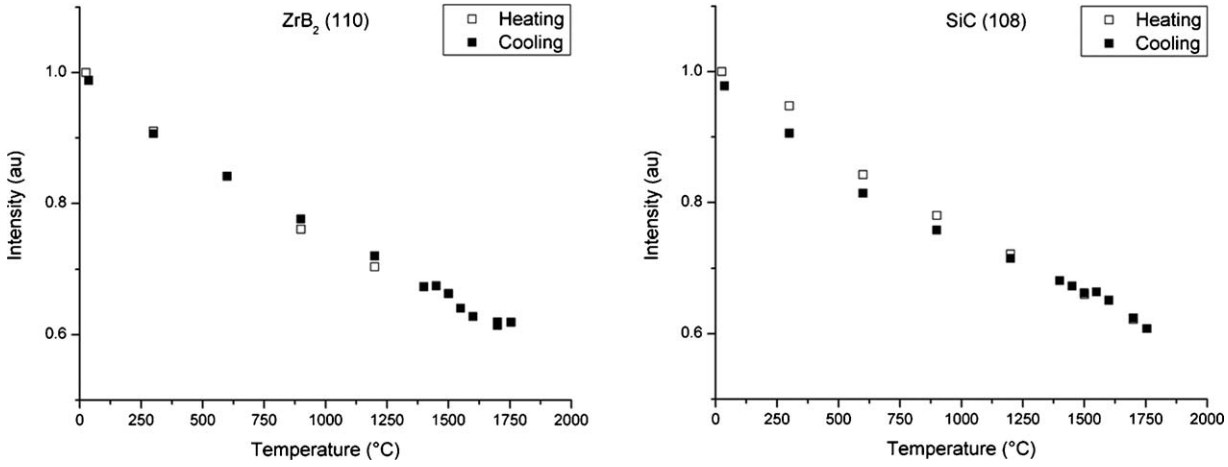

Fig. 3. Neutron diffraction intensity as a function of temperature for representative $Zr^{11}B_2$ and SiC planes showing that the change in intensity between heating and cooling was negligible.

ticular by the high vacuum ($\sim 1.3 \times 10^{-3}$ Pa) conditions during testing. The temperatures of the experiment combined with the atmospheric pressure fall into a regime where SiC is known to actively oxidize.[34–36] As a result, SiC particles near the specimen surface underwent active oxidation leaving a surface layer of $\sim$50 μm that was depleted of SiC (Fig. 2). The transition between the SiC depleted layer and the normal microstructure remained sharp. While a decrease in the amount of SiC taking part in the neutron diffraction should result in diminished peak intensity, the thickness of the depleted layer represents a small volume of material in comparison to the overall specimen. Based on the thickness of the SiC depleted layer, approximately 4.5 vol% of the SiC was lost. While this would result in a small decrease in the diffracted intensities, the loss of SiC would not affect the peak positions and, therefore, should not impact the analysis of residual stresses.

The change in intensity of a diffracted peak as a function of temperature is governed by the Debye–Waller factor. The intensity should decrease as temperature increases due to increased thermal vibrations. This change, however, is completely reversible and as the specimen is cooled the intensity should return to its original value. Deviation from this behavior is an indication that the quantity of the phase in question has been altered during the experiment; whether by reaction, oxidation, or some other means. Plotting intensity as a function of temperature for representative peaks from $Zr^{11}B_2$ and SiC, the (1 1 0) and (1 0 8), respectively, revealed that the change in intensity as a function of temperature was completely reversible (Fig. 3). The other crystallographic directions show the same behavior. The slight difference in diffracted intensities ($\sim$4%) between heating and cooling of the SiC is consistent with the loss of a small amount of SiC due to active oxidation as discussed earlier.

Initially, single peak fitting was performed on peaks in both the composite and powder samples using only peaks that exhibited no overlap with peaks from the other phase or the Nb container used for the powder samples. This was done in an effort to minimize any potential error due to interference between peaks. Examples of the peak fits for the $Zr^{11}B_2$ (1 1 0) and SiC (0 0 6) reflection (Fig. 4) illustrate the isolated peaks used for data fitting. The plus symbols represent the actual data points with a curve representing a smooth fit passing through the data. The lower line in the plots is a measure of the error between the actual data and the position of the fit curve. The fits obtained using this method produced data that could be used to calcu-

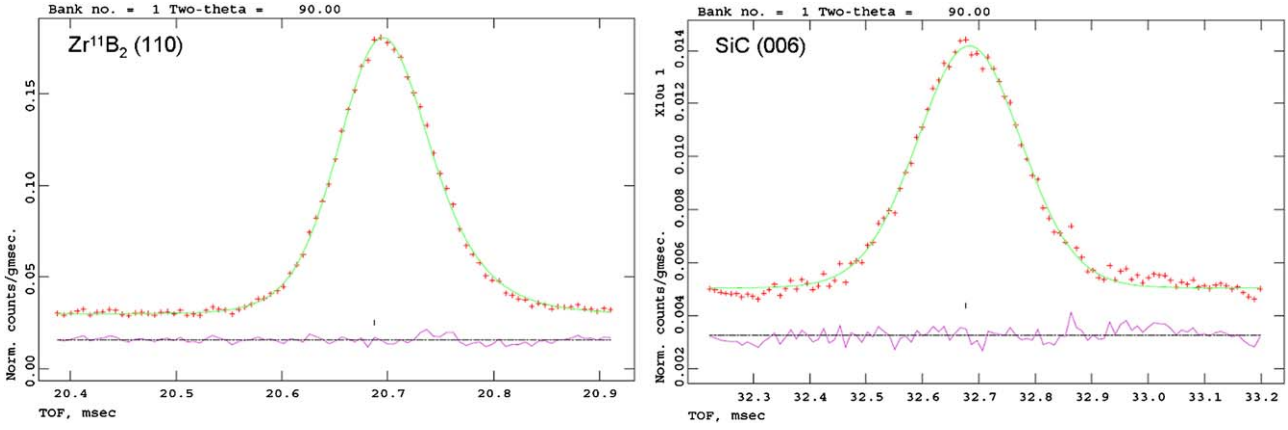

Fig. 4. Single peak fits for $Zr^{11}B_2$ (1 1 0) and SiC (0 0 6) reflections obtained by neutron diffraction showing actual data points (plus symbols), the fit line (smooth curve), and the error associated with the fit (bottom line).

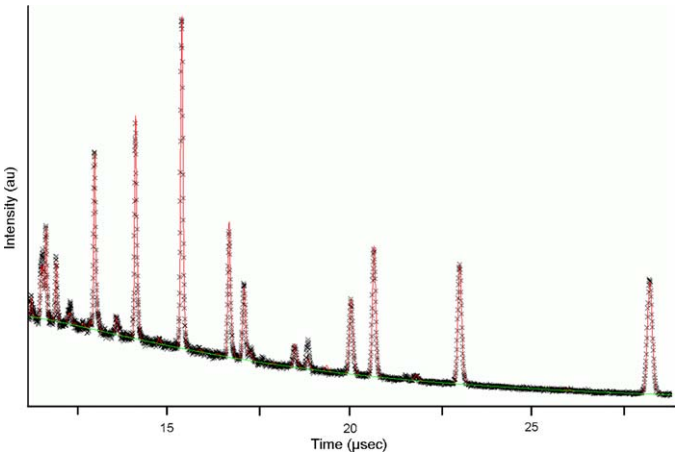

Fig. 5. A representative full pattern fit of a $Zr^{11}B_2$–SiC composite where X's denote real data with the solid curve representing the full pattern fit.

late stresses; however, only two peaks from each phase could be fit due to overlap of the other peaks. The stressed positions of the SiC (0 0 6) and $Zr^{11}B_2$ (1 1 0) peaks were found to be 2.50817 ± 0.0001 Å and 1.5853 ± 0.0001 Å, respectively. To calculate stresses based on more crystallographic reflections, full pattern fitting was then also employed (Fig. 5). Rietveld refinements resulted in fits with reduced chi^2 values below 3. Following refinement, each pattern was visually inspected to ensure that the background fit was not overparameterized.

To gauge the accuracy of the full pattern fitting, the available single peak fits were compared to their counterparts in the full pattern fitting. The SiC (0 0 6) d-spacing obtained at room temperature from the full pattern fit was the same as that obtained by the single peak fit to within 0.0001 Å, which was at the resolution of this measurement. The $Zr^{11}B_2$ (1 1 0) d-spacing was different by only 0.0004 Å. This close agreement between techniques indicated that the full pattern fitting was able to fit the individual peaks with the same precision as the single peak method. As a result all calculations have been performed using data gathered from full pattern fitting.

The residual stresses present in the $Zr^{11}B_2$–SiC composites were calculated by comparing the lattice parameters of $Zr^{11}B_2$ and SiC from the composite with those of pure powders, which were assumed to be stress free. The strain (ε) in the composite was calculated by dividing the difference in lattice parameter (ΔL) between the composite and powder by the lattice parameter of the stress free powder (L_o), which was assumed to be unaltered by stress ($\varepsilon = \Delta L/L_o$). By knowing the elastic modulus (E) of the material as a function lattice direction, the stress (σ) can then be calculated ($\sigma = E\varepsilon$). Because the strains, and therefore the calculated stresses, are specific to a given crystallographic direction, the average elastic modulus of the material is not sufficient for the calculation of the directionally dependent stresses. Instead, the elastic modulus specific to each crystallographic direction must be used (E_{hkl}), which requires use of the full elastic matrix. Since ZrB_2 and α-SiC have hexagonal crystal structures, they each have five independent stiffness coefficients as shown in the elastic stiffness matrix (Eq. (1)). The values of each stiffness coefficient for both ZrB_2 and SiC are given in Table 1.[37]

Table 1
The five independent stiffness coefficients for ZrB_2 and SiC.

Material	c_{ij} (GPa)					Reference
	c_{11}	c_{12}	c_{13}	c_{33}	c_{44}	
ZrB_2	567.8	26.9	120.5	436.1	247.5	[45]
SiC	511.7	112.6	53.3	565.2	167.6	[46]

$$\begin{pmatrix} c_{11} & c_{12} & c_{13} & 0 & 0 & 0 \\ c_{12} & c_{11} & c_{13} & 0 & 0 & 0 \\ c_{13} & c_{13} & c_{33} & 0 & 0 & 0 \\ 0 & 0 & 0 & c_{44} & 0 & 0 \\ 0 & 0 & 0 & 0 & c_{44} & 0 \\ 0 & 0 & 0 & 0 & 0 & \frac{1}{2}(c_{11} - c_{12}) \end{pmatrix} \quad (1)$$

Using an equation developed by Zhang et al.[38] the elastic modulus, E_{hkl}, related to any crystallographic direction in a hexagonal crystal can be calculated from Eq. (2).[38]

$$E_{hkl} = \frac{[h^2 + ((h+2k)^2/3) + (al/c)^2]^2}{s_{11}(h^2 + ((h+2k)^2/3))^2 + s_{33}(al/c)^4 + (2s_{13} + s_{44})(h^2 + ((h+2k)^2/3))(al/c)^2} \quad (2)$$

where s_{11}, s_{12}, s_{13}, s_{33}, and s_{44} represent the compliance coefficients for a hexagonal crystal, h, k, and l are the Miller indices of the desired crystallographic direction, and a and c are lattice parameters. The a and c lattice parameters for ZrB_2 are 3.168 Å and 3.530 Å (JCPDS card no. 34-0423), respectively, while those for SiC are 3.073 Å and 15.080 Å (JCPDS card no. 29-1131), respectively. The compliance coefficients of both ZrB_2 and SiC needed for Eq. (2) were calculated from the known stiffness coefficients using Eqs. (3)–(8).[37]

$$c_{11} + c_{12} = \frac{s_{33}}{S} \quad (3)$$

$$c_{11} - c_{12} = \frac{1}{s_{11} - s_{12}} \quad (4)$$

$$c_{13} = \frac{-s_{13}}{S} \quad (5)$$

$$c_{33} = \frac{s_{11} + s_{12}}{S} \quad (6)$$

$$c_{44} = \frac{1}{s_{44}} \quad (7)$$

$$S = s_{33}(s_{11} + s_{12}) - 2s_{13}^2 \quad (8)$$

Solving Eqs. (3)–(8) simultaneously and using the stiffness coefficients from Table 1, yielded the compliance coefficients for both ZrB_2 and SiC (Table 2).

Table 2
The five independent compliance coefficients for ZrB_2 and SiC.

Material	s_{ij} (GPa^{-1})				
	s_{11}	s_{12}	s_{13}	s_{33}	s_{44}
ZrB_2	1.88E−03	−8.28E−05	−4.95E−04	2.57E−03	4.04E−03
SiC	2.07E−03	−4.39E−04	−1.54E−04	1.80E−03	5.97E−03

Table 3
Elastic modulus, strain, and compressive stress in the SiC phase of a $Zr^{11}B_2$–SiC composite for seven crystallographic directions.

(*h k l*)	E_{hkl} (GPa)	ε	σ (MPa)
1 0 0	484	1.94E−03	937
1 0 1	474	1.94E−03	918
0 0 6	556	1.51E−03	842
1 0 2	452	1.93E−03	872
1 0 8	437	1.87E−03	820
1 1 0	484	1.94E−03	939
1 1 6	426	1.92E−03	815

Using Eq. (2), the Miller indices of given directions for SiC and $Zr^{11}B_2$, and the compliance coefficients in Table 2, the elastic moduli were calculated for seven individual crystallographic directions for both SiC and $Zr^{11}B_2$ as shown in Tables 3 and 4, respectively. Also in Tables 3 and 4 are the stresses calculated for those crystallographic directions in both SiC and $Zr^{11}B_2$. These calculations indicate an average compressive stress within the SiC of ~880 MPa and a corresponding average tensile stress within the $Zr^{11}B_2$ of ~450 MPa for composites cooled to room temperature. In a composite such as this, the stresses within the two phases must be balanced. That is to say that using the rule of mixtures, the sum of the stresses, weighted according to volume fraction of each phase, must sum to zero. Starting with the nominal SiC content of 30 vol% and the average measured compressive stress of 880 MPa, the tensile stress in the $Zr^{11}B_2$ would be expected to be ~380 MPa, which is only 70% of what was measured. However, the initial powders were attrition milled using SiC milling media. As a result, erosion of the media during milling added to the total amount of SiC within the composite. Performing areal analysis of SEM micrographs of the composite revealed that the SiC content comprised ~34 vol% of the composite and not 30 vol% as expected based on the starting powder composition. This analysis was based on the measurement of ~1000 SiC particles from 5 SEM images similar to those in Fig. 1. Contamination from milling is common in ceramic processing, which is why SiC milling media were selected for this study to prevent the introduction of additional components into the system. Using 34 vol% SiC and its average compressive stress of 880 MPa, the tensile stress in the $Zr^{11}B_2$ was estimated to be ~450 MPa using the rule of mixtures calculation, which agrees with the neutron diffraction measurements that predicted an average tensile stress of ~450 MPa.

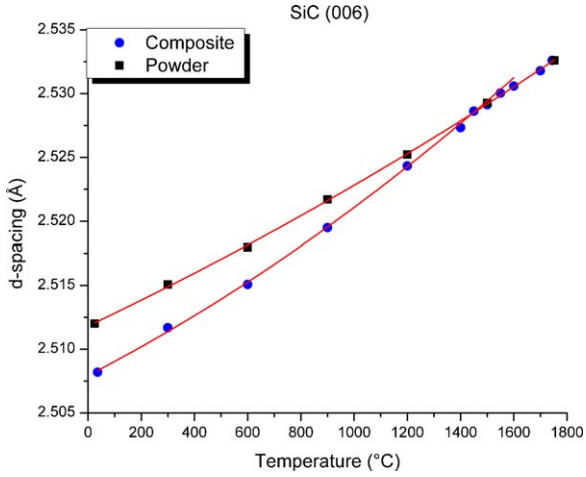

Fig. 6. Measured d-spacing as a function of temperature for the SiC (0 0 6) peaks for both the composite and pure powder as measured by neutron diffraction along with a fit curves.

Neutron diffraction data was also analyzed to determine the temperature at which stresses began to accumulate during cooling. Figs. 6 and 7 are representative plots of the d-spacings as a function of temperature for SiC (Fig. 6) and $Zr^{11}B_2$ (Fig. 7) in the composite and as pure powders. The (006) planes of SiC in both the composite and powder had the same d-spacing at elevated temperature (Fig. 6). Because diffusional mechanisms which can relax stresses become active as temperatures increase, it follows that the composite should be stress free above some critical temperature. Diffusional creep in the ZrB_2 matrix as well as grain boundary sliding in SiC have been observed at temperatures as

Table 4
Elastic modulus, strain, and tensile stress in the $Zr^{11}B_2$ phase of a $Zr^{11}B_2$–SiC composite for seven crystallographic directions.

(*h*	*k*	*l*)	E_{hkl} (GPa)	ε	σ (MPa)
1	0	1	553	−9.00E−04	498
0	0	2	390	−7.18E−04	280
1	1	0	533	−1.01E−03	540
1	1	1	557	−9.61E−04	535
1	1	2	544	−8.80E−04	478
3	0	0	533	−1.01E−03	539
1	0	4	419	−7.45E−04	313

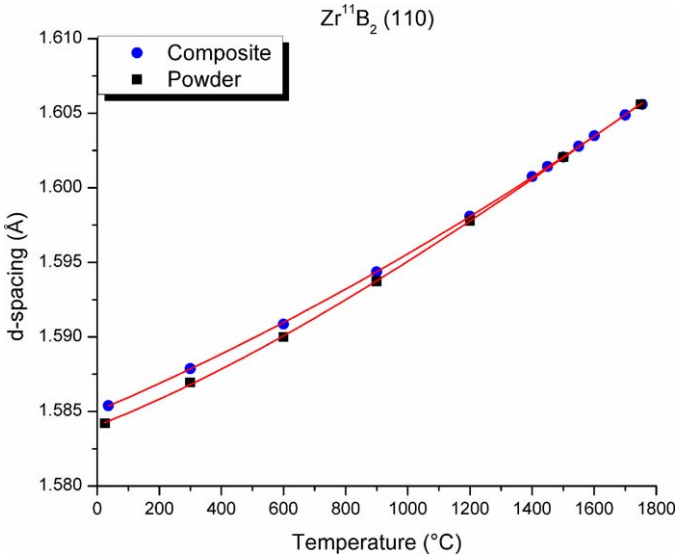

Fig. 7. Measured d-spacing as a function of temperature for the $Zr^{11}B_2$ (1 1 0) peaks for both the composite and the powder as measured by neutron diffraction along with a fit curves.

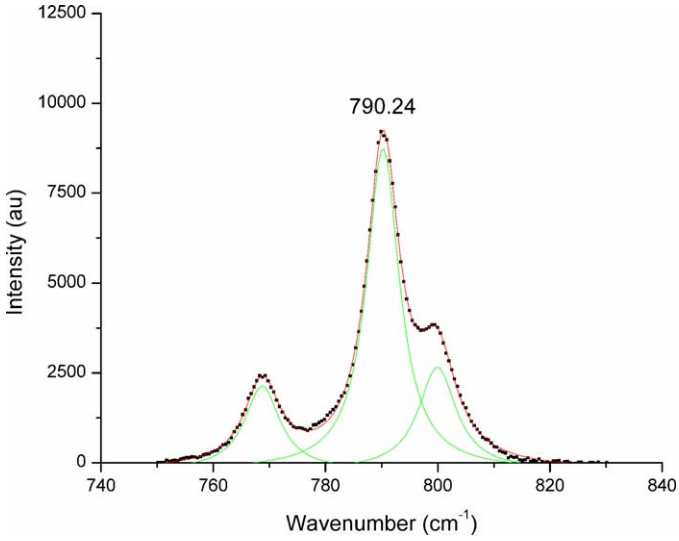

Fig. 8. Raman pattern of a SiC grain within the $Zr^{11}B_2$–SiC composite along with deconvoluted peak fits and peak position for the TO peak.

low as 1200 °C at 100 MPa stress in ZrB_2–SiC composites.[39] At 1200 °C and below, the d-spacings were no longer the same, indicating the development of strain in the SiC lattice and, therefore, residual stresses. Fig. 7 illustrates the same behavior from the $Zr^{11}B_2$ (1 1 0) planes. At elevated temperature the lattice parameters of the powder and the composite were the same, but at 1200 °C and below they deviated. To estimate the temperature at which stresses began to accumulate, the powder d-spacing data were fitted with a second order polynomial. Likewise, the composite d-spacing data were fitted from 1200 °C and below to another second order polynomial. The fit to the composite d-spacing data was then extrapolated to higher temperatures until it intercepted the fit for the powder data. The two fit curves for both the SiC (0 0 6) and the $Zr^{11}B_2$ (1 1 0) intercepted one another at ~1400 °C (Figs. 6 and 7). Similar analyses have been performed for other crystallographic planes in both SiC and $Zr^{11}B_2$, all of which indicated that stresses began to accumulate at ~1400 °C as the composite was cooled. Due to the fact that stress relaxation above 1400 °C is likely based on diffusional mechanisms it is expected that all the crystallographic directions would behave similarly.

Stress measurement via neutron diffraction yielded an average stress over the entire sample due to the ability of the neutrons to penetrate through the specimens. For comparison, Raman spectroscopy performed in this study utilized a small spot size (~1 μm) and was expected to have only probed the top ~100 nm of the surface of the sample due to the laser wavelengths employed.[40,41] As a result, Raman spectroscopy was able to probe the stresses in a single grain per measurement. Unfortunately, ZrB_2 is not Raman active; therefore stress measurements could only be performed on the SiC phase. Several peaks are associated with 6H SiC in Raman spectroscopy; the 2 main peaks are the transverse optic (TO) peak at 789.2 cm^{-1} and the linear optic (LO) peak at 970.1 cm^{-1}.[26] These peak positions are sensitive to stress. While no general relationship has been determined to relate Raman peak shift to stress, researchers have measured peak shifts as a function of applied stress for a variety of materials including 6H SiC. Liu and Vohra measured the peak position of single crystals of 6H SiC as a function of applied pressure up to 95 GPa.[26] By doing so they were able to develop a correlation between the position of the TO peak and stress (Eq. (9)),[26]

$$\omega_{TO}(cm^{-1}) = 789.2 + 3.11P - 0.009P^2 \quad (9)$$

where ω_{TO} is the measured peak position and P is the hydrostatic stress in GPa. In the present study, the position of the TO peak was measured by acquiring a Raman pattern from ~740 to 840 cm^{-1} and fitting the resultant peaks (Fig. 8). Because of overlap between the TO peak and those surrounding it, the overall curve was deconvoluted to fit the individual peaks that comprise it. The central peak in Fig. 8 is the TO peak, which as found to be at 790.24 cm^{-1}. Inputting this value as ω_{TO} in Eq. (9) and solving for P results in a compressive stress of 335 MPa. While Fig. 8 is representative of the Raman patterns, a range of stress values were measured. The average stress measured was 390 MPa; values ranged from 235 MPa to 595 MPa with a standard deviation of 100 MPa for 25 SiC grains measured to obtain these values. Assuming the cross section that was examined contained a random selection of SiC particles, some of the particles would be expected to be the top of larger particles that were predominantly below the surface. Others would be only the tips of particles that were almost completely removed by sectioning and polishing, while others would cover the range in between those two extremes. As a result, it is expected that the Raman peak shifts would provide a range of stresses when measuring individual particles as they were constrained differently depending on how much of each particle lay below the surface. The average stress of 390 MPa estimated from Raman peak shifts was only ~40% of the stress determined using neutron diffraction (880 MPa). Lower stresses can be expected from particles on the surface that were probed by Raman spectroscopy

Table 5
Mass absorption coefficients and densities necessary to calculate x-ray penetration depth assuming a Cu Kα source.[39]

Absorber	ρ (g/cm^3)	μ/ρ (cm^2/g)
Zr	6.51	136.8
B	2.47	2.142
Si	2.33	65.32
C	2.27	4.219

as compared to particles in the bulk that were probed by neutron diffraction. Modeling in Al_2O_3–Al particle reinforced composites suggests that compressive stresses in particles on and near the surface are less than those of particles in the bulk due to decreased confinement by the matrix.[42]

To further evaluate the stresses in particles near the surface of the composite, grazing incidence x-ray diffraction was performed. Since Raman only measures particles within ~100 nm of the surface, the angle of incidence for the x-ray beam was set at 1° relative to the surface to control the depth of penetration of the x-ray beam. The mass absorption coefficient, μ, and the geometry of the diffractometer govern the depth of penetration of an x-ray beam into a specimen. This relationship is given in Eq. (10) where θ is one half the diffraction angle 2θ, and G_x is the fraction of the total diffracted intensity supplied by a surface layer of thickness x (cm).[43]

$$G_x = 1 - e^{(-2\mu x/\sin\theta)} \tag{10}$$

When dealing with a composite or a compound, the value for μ in Eq. (10) is a mass average of the constituents (Eq. (11)), where w_i is the weight fraction and ρ_i the density of the individual components of the composite or compound.[43]

$$\frac{\mu}{\rho} = w_1\left(\frac{\mu}{\rho}\right)_1 + w_2\left(\frac{\mu}{\rho}\right)_2 \tag{11}$$

Using Eq. (11), the appropriate μ/ρ values were calculated for both ZrB_2 and SiC, which were then used to calculate μ for the composite for use in Eq. (10). Using the values presented in Table 5, an angle of incidence of 1°, and a fraction of the total diffracted intensity of 95%, the depth of penetration, x, was calculated to be ~1 μm. This calculation suggests that 95% of the total diffracted intensity came from a layer on the surface of the composite that was 1 μm thick. Hence, stresses measured using grazing incidence x-ray diffraction and Raman Spectroscopy should be similar. X-ray diffraction patterns for both the composite material and pure SiC powder were collected (Fig. 9). Comparing the d-spacings of the SiC peaks present in both the composite and powder samples (Fig. 9) showed that the SiC peaks in the composite were shifted to higher 2θ values, which correspond to a smaller d-spacing and thus, a compressive stress. As discussed above, the difference in d-spacing for each peak was used to calculate strain, and the appropriate E_{hkl} were then used to calculate stresses in each individual crystallographic direction. Based on the average of the individual crystallographic directions the compressive stress in SiC as determined by grazing incidence x-ray diffraction was ~350 MPa. This is in close

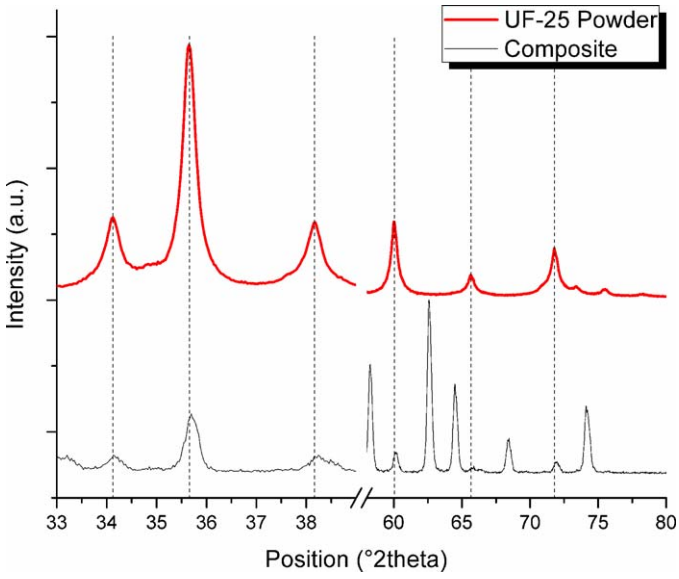

Fig. 9. Grazing incidence x-ray pattern of both pure UF-25 SiC powder as well as the $Zr^{11}B_2$–SiC composite showing the SiC peaks in the composite pattern have shifted to higher 2θ.

agreement with the 390 MPa average compressive stress measured by Raman spectroscopy.

The presence of tensile stresses in the brittle matrix of a particulate reinforced composite such as ZrB_2–SiC could be expected to decrease the strength of the composite as compared to the nominally pure matrix material. However, additions of SiC particles to ZrB_2 have been shown to increase the strength of the composite.[4–7] The strengthening effect can be explained, in part, through analysis that uses the Griffith equation (Eq. (12)),[44]

$$\sigma = \frac{K_{IC}}{Y\sqrt{c}} \tag{12}$$

where σ is the failure strength, K_{IC} is the mode one fracture toughness, c is the flaw size, and Y is a geometric parameter dependent on flaw shape. Given this relationship, increasing the fracture toughness should increase the failure strength proportionally assuming that the geometric parameter and flaw size are not affected. Additions of SiC to ZrB_2 have been shown to increase the fracture toughness from ~3.5 MPa·m$^{1/2}$ for monolithic ZrB_2[4] to as much as 6 MPa·m$^{1/2}$.[7] The relationship, however, is more complex than simply doubling the fracture toughness since the addition of SiC particles to ZrB_2 also decreases the critical flaw size,[5,6] c, as well as inducing thermal residual stresses. This analysis does indicate that the possible reduction in strength due to tensile stresses in the matrix can be more than overcome by the increase in strength due to increased fracture toughness and decreased critical flaw size. This also means that if the tensile stresses generated in the ZrB_2 matrix during processing could be reduced without changing the grain size or sacrificing fracture toughness, the strength might be further improved over the monolith and the composite.

4. Conclusions

A $Zr^{11}B_2$–SiC composite was produced using isotopically enriched boron-11 to facilitate the use of neutron diffraction to characterize residual stresses. Neutron diffraction patterns were collected at regular temperature intervals from room temperature up to 1750 °C. By comparing the d-spacings of $Zr^{11}B_2$ and SiC in the composite to their pure powder counterparts, it was determined that stresses within the composite begin to accumulate at ~1400 °C during cooling. Total accumulated stresses within the composite at room temperature were 880 MPa compression in the SiC particle phase, and 450 MPa tension in the $Zr^{11}B_2$ matrix. Both Raman spectroscopy and x-ray diffraction were used to provide complementary measurements. Both determined that the stresses on the surface of the composite were ~40% of those present in the bulk. Stress measurements using Raman spectroscopy showed the compressive stress in the SiC particulate phase to be 390 MPa while measurements performed using grazing incidence x-ray diffraction show it to be 350 MPa. Stresses in the bulk as well as on the surface of ZrB_2–SiC composites were successfully measured using a combination of neutron diffraction, x-ray diffraction and Raman spectroscopy. While the addition of 30 vol% SiC particles to ZrB_2 resulted in a tensile stress of ~450 MPa in the ZrB_2 matrix it did not decrease the strength of the composite but instead increased it. This is due in part to the increase in fracture toughness and decrease in grain size that the SiC particles impart to the composite. The increase in strength through the addition of SiC may be improved further if the matrix tensile stresses can be reduced.

Acknowledgements

This work has benefited from the use of the Lujan Neutron Scattering Center at LANSCE, which is funded by the Office of Basic Energy Sciences (DOE).

Los Alamos National Laboratory is operated by Los Alamos National Security LLC under DOE Contract DE AC52 06NA25396. Research at Missouri S&T was supported by the High Temperature Aerospace Materials Program (Drs. Joan Fuller and Ali Sayir, program managers) in the Air Force Office of Scientific Research through grant FA9550-09-1-0168.

References

1. Cutler RA. Engineering properties of borides. In: Schneider Jr SJ, editor. *Ceramics and glasses, engineered materials handbook*, vol. 4. Materials Park, OH: ASM International; 1991. p. 787–803.
2. Fahrenholtz WG, Hilmas GE, Talmy IG, Zaykoski JA. Refractory diborides of zirconium and hafnium. *J Am Ceram Soc* 2007;**90**(5):1347–64.
3. Mishra SK, Das S, Das SK, Ramachandrarao P. Sintering studies on ultrafine ZrB_2 powder produced by a self-propagating high-temperature synthesis process. *J Mater Res* 2000;**15**(11):2499–504.
4. Chamberlain AL, Fahrenholtz WG, Hilmas GE, Ellerby DT. High-strength zirconium diboride-based ceramics. *J Am Ceram Soc* 2004;**87**(6):1170–2.
5. Rezaie A, Fahrenholtz WG, Hilmas GE. Effect of hot pressing time and temperature on the microstructure and mechanical properties of ZrB_2–SiC. *J Mater Sci* 2007;**42**(8):2735–44.
6. Zhu S, Fahrenholtz WG, Hilmas GE. Influence of silicon carbide particle size on the microstructure and mechanical properties of zirconium diboride–silicon carbide ceramics. *J Eur Ceram Soc* 2007;**27**(4):2077–83.
7. Liu Q, Han W, Zhang X, Wang S, Han J. Microstructure and mechanical properties of ZrB_2–SiC composites. *Mater Lett* 2009;**63**(15):1323–5.
8. Chamberlain A, Fahrenholtz W, HIlmas G, Ellerby D. Oxidation of ZrB_2–SiC ceramics under atmospheric and reentry conditions. *Refract Appl Trans* 2004;**1**(2):2–8.
9. Fahrenholtz WG. Thermodynamic analysis of ZrB_2–SiC oxidation: formation of a SiC-depleted region. *J Am Ceram Soc* 2007;**90**(1):143–8.
10. Monteverde F, Scatteia L. Resistance to thermal shock and to oxidation of metal diborides–SiC ceramics for aerospace application. *J Am Ceram Soc* 2007;**90**(4):1130–8.
11. Peng F, Speyer RF. Oxidation resistance of fully dense ZrB_2 with SiC, TaB_2, and $TaSi_2$ additives. *J Am Ceram Soc* 2008;**91**(5):1489–94.
12. Rezaie A, Fahrenholtz WG, Hilmas GE. Oxidation of zirconium diboride–silicon carbide at 1500 °C at a low partial pressure of oxygen. *J Am Ceram Soc* 2006;**89**(10):3240–5.
13. Talmy IG, Zaykoski JA, Opeka MM. High-temperature chemistry and oxidation of ZrB_2 ceramics containing SiC, Si_3N_4, Ta_5Si_3, and $TaSi_2$. *J Am Ceram Soc* 2008;**91**(7):2250–7.
14. Zimmermann JW, Hilmas GE, Fahrenholtz WG, Dinwiddie RB, Porter WD, Wang H. Thermophysical properties of ZrB_2 and ZrB_2–SiC ceramics. *J Am Ceram Soc* 2008;**91**(5):1405–11.
15. Jackson TA, Eklund DR, Fink AJ. High speed propulsion: performance advantage of advanced materials. *J Mater Sci* 2004;**39**(19):5905–13.
16. Opeka MM, Talmy IG, Zaykoski JA. Oxidation-based materials selection for 2000 °C + hypersonic aerosurfaces: theoretical considerations and historical experience. *J Mater Sci* 2004;**39**(19):5887–904.
17. Van Wie DM, Drewry DG, King DE, Hudson CM. The hypersonic environment: required operating conditions and design challenges. *J Mater Sci* 2004;**39**(19):5915–24.
18. Touloukian YC, Ho C, Dewitt D. In: Touloukian, editor. *Thermal expansion: nonmetallic solids*, vol. 13. New York: IFI/Plenum; 1977. p. 1970.
19. Bartolomé JF, Bruno G, DeAza AH. Neutron diffraction residual stress analysis of zirconia toughened alumina (ZTA) composites. *J Eur Ceram Soc* 2008;**28**(9):1809–14.
20. Todd RI, Bourke MAM, Borsa CE, Brook RJ. Neutron diffraction measurements of residual stresses in alumina/SiC nanocomposites. *Acta Mater* 1997;**45**(4):1791–800.
21. Wain N, Radaelli PG, Todd RI. In situ neutron diffraction study of residual stress development in MgO/SiC ceramic nanocomposites during thermal cycling. *Acta Mater* 2007;**55**(13):4535–44.
22. Watts J, Hilmas G, Fahrenholtz WG, Brown D, Clausen B. Stress measurements in ZrB_2–SiC composites using Raman spectroscopy and neutron diffraction. *J Eur Ceram Soc* 2010;**30**(11):2165–71.
23. Withers PJ. Depth capabilities of neutron and synchrotron diffraction strain measurement instruments. II. Practical implications. *J Appl Crystallogr* 2004;**37**:607–12.
24. Skoog, Holler, Nieman, editors. *Principals of instrumental analysis*, vol. 5. Philadelphia: Harcourt Brace; 1998. p. 429–35.
25. Ghosh D, Subhash G, Orlovskaya N. Measurement of scratch-induced residual stress within SiC Grains in ZrB_2–SiC composite using micro-Raman spectroscopy. *Acta Mater* 2008;**56**(18):5345–54.
26. Liu J, Vohra YK. Raman modes of 6H polytype of silicon carbide to ultrahigh pressures: a comparison with silicon and diamond. *Phys Rev Lett* 1994;**72**(26):4105.
27. Salvador G, Sherman WF. Pressure dependence of the Raman phonon spectrum in 6h-silicon carbide. *J Mol Struct* 1991;**247**:373–84.
28. Wu X, Yu J, Ren T, Liu L. Micro-Raman spectroscopy measurement of stress in silicon. *Microelectron J* 2007;**38**(1):87–90.
29. Young RJ, Buschow KHJ, Robert WC, Merton CF, Bernard I, Edward JK, et al. Residual stresses: measurement by Raman shift. In: *Encyclopedia of materials: science and technology.* Oxford: Elsevier; 2001. p. 8170–2.
30. Ohtsuka S, Zhu W, Tochino S, Sekiguchi Y, Pezzotti G. In-depth analysis of residual stress in an alumina coating on silicon nitride substrate using confocal Raman piezo-spectroscopy. *Acta Mater* 2007;**55**(4):1129–35.
31. Olego D, Cardona M, Vogl P. Pressure dependence of the optical phonons and transverse effective charge in 3C–SiC. *Phys Rev B* 1982;**25**(6):3878.

32. Sears VF. Neutron scattering length and cross sections. *Neutron News* 1992;**3**(3):26–37.
33. Larson AC, Von Dreele RB, General Structure Analysis System (GSAS) [computer program], Los Alamos National Laboratory Report LAUR 86-748; 2000.
34. Charpentier L, Balat-Pichelin M, Glénat H, Bêche E, Laborde E, Audubert F. High temperature oxidation of SiC under helium with low-pressure oxygen. Part 2: CVD [beta]-SiC. *J Eur Ceram Soc* 2010;**30**(12): 2661–70.
35. Goto T, Homma H. High-temperature active/passive oxidation and bubble formation of CVD SiC in O_2 and CO_2 atmospheres. *J Eur Ceram Soc* 2002;**22**(14–15):2749–56.
36. Hatta H, Aoki T, Kogo Y, Yarii T. High-temperature oxidation behavior of SiC-coated carbon fiber-reinforced carbon matrix composites. *Composites Part A: Appl Sci Manuf* 1999;**30**(4):515–20.
37. Newnham R. *Properties of materials*. New York: Oxford University Press Inc.; 2005. p. 378.
38. Zhang J-M, Zhang Y, Xu K-W, Ji V. General compliance transformation relation and applications for anisotropic hexagonal metals. *Solid State Commun* 2006;**139**(3):87–91.
39. Talmy IG, Zaykoski JA, Martin CA. Flexural creep deformation of ZrB_2/SiC ceramics in oxidizing atmosphere. *J Am Ceram Soc* 2008;**91**(5):1441–7.
40. Havel M, Colomban P. Rayleigh and Raman images of the bulk/surface nanostructure of SiC based fibres. *Composites Part B: Eng* 2004;**35**(2):139–47.
41. Liu H, Cheng H, Wang J, Tang G, Che R, Ma Q. Effects of the fiber surface characteristics on the interfacial microstructure and mechanical properties of the KD SiC fiber reinforced SiC matrix composites. *Mater Sci Eng: A* 2009;**525**(1–2):121–7.
42. Borbély A, Biermann H, Hartmann O, Buffière JY. The influence of the free surface on the fracture of alumina particles in an Al–Al_2O_3 metal–matrix composite. *Comput Mater Sci* 2003;**26**:183–8.
43. Cullity BD. *Elements of X-ray diffraction*. Reading, Massachusetts: Addison-Wesley; 1978. p. 555.
44. Wachtman J. *Mechanical properties of ceramics*. New York: John Wiley & Sons, Inc.; 1996. p. 56.
45. Okamoto NL, Kusakari M, Tanaka K, Inui H, Yamaguchi M, Otani S. Temperature dependence of thermal expansion and elastic constants of single crystals of ZrB_2 and the suitability of ZrB_2 as a substrate for GaN film. *J Appl Phys* 2003;**93**(1):88–93.
46. Yao H, Ouyang L, Ching WY. Ab initio calculation of elastic constants of ceramic crystals. *J Am Ceram Soc* 2007;**90**(10):3194–204.